UNIVERSITÄT AUGSBURG
Universitätsbibliothek

OPEN ACCESS
OPUS AUGSBURG

Validation of GBS plasma turbulence simulation of the TJ-K stellarator

A. J. Coelho, J. Loizu, P. Ricci, M. Ramisch, A. Köhn-Seemann, Gregor Birkenmeier, K. Rahbarnia

Angaben zur Veröffentlichung / Publication details:

Coelho, A. J., J. Loizu, P. Ricci, M. Ramisch, A. Köhn-Seemann, Gregor Birkenmeier, and K. Rahbarnia. 2023. "Validation of GBS plasma turbulence simulation of the TJ-K stellarator." *Plasma Physics and Controlled Fusion* 65 (8): 085018. https://doi.org/10.1088/1361-6587/ace4f3.

Nutzungsbedingungen / Terms of use:

CC BY 4.0

Dieses Dokument wird unter folgenden Bedingungen zur Verfügung gestellt: / This document is made available under these conditions:
CC-BY 4.0: Creative Commons: Namensnennung
Weitere Informationen finden Sie unter: / For more information see:
https://creativecommons.org/licenses/by/4.0/deed.de

Plasma Physics and
Controlled Fusion

PURPOSE-LED
PUBLISHING™

PAPER • OPEN ACCESS

Validation of GBS plasma turbulence simulation of the TJ-K stellarator

To cite this article: A J Coelho *et al* 2023 *Plasma Phys. Control. Fusion* **65** 085018

View the article online for updates and enhancements.

You may also like

- Global fluid simulation of plasma turbulence in a stellarator with an island divertor
A.J. Coelho, J. Loizu, P. Ricci et al.
- Global fluid simulation of plasma turbulence in stellarators with the GBS code
A.J. Coelho, J. Loizu, P. Ricci et al.
- Edge turbulence in tokamaks, stellarators and reversed field pinches
A J Wootton, H Y W Tsui and S Prager

This content was downloaded from IP address 137.250.102.76 on 04/11/2026 at 09:17

OPEN ACCESS
IOP Publishing
Plasma Physics and Controlled Fusion
Plasma Phys. Control. Fusion **65** (2023) 085018 (12pp)
https://doi.org/10.1088/1361-6587/ace4f3

Validation of GBS plasma turbulence simulation of the TJ-K stellarator

A J Coelho[1,*], J Loizu[1], P Ricci[1], M Ramisch[2], A Köhn-Seemann[2], G Birkenmeier[3,4] and K Rahbarnia[5]

[1] Ecole Polytechnique Fédérale de Lausanne (EPFL), Swiss Plasma Center (SPC), CH-1015 Lausanne, Switzerland
[2] Institute of Interfacial Process Engineering and Plasma Technology IGVP, University of Stuttgart, 70569 Stuttgart, Germany
[3] Max Planck Institute for Plasma Physics, Boltzmannstr. 2, 85748 Garching, Germany
[4] Physik-Department E28, Technische Universität München, James-Franck-Str. 1, 85748 Garching, Germany
[5] Max Planck Institute for Plasma Physics, 17491 Greifswald, Germany

E-mail: antonio.coelho@epfl.ch

Received 30 March 2023, revised 19 June 2023
Accepted for publication 6 July 2023
Published 14 July 2023

Abstract

We present a validation of a three-dimensional, two-fluid simulation of plasma turbulence in the TJ-K stellarator, a low temperature plasma experiment ideally suited for turbulence measurements. The simulation is carried out by the GBS code, recently adapted to simulate 3D magnetic fields. The comparison shows that GBS retrieves the main turbulence properties observed in the device, namely the fact that transport is dominated by fluctuations with low poloidal mode number. The poloidal dependence of the radial $E \times B$ turbulent flux is compared on a poloidal plane with elliptical flux surfaces, where a very good agreement between experiment and simulation is observed, and on another with triangular flux surfaces, which shows a poorer comparison. The fluctuation levels in both cases are underestimated in the simulations. The equilibrium density profile is well retrieved by the simulation, while the electron temperature and the electrostatic potential profiles, which are very sensitive to the strength and localization of the sources, do not agree well with the experimental measurements.

Keywords: validation of simulation, TJ-K stellarator, GBS code, turbulence

(Some figures may appear in colour only in the online journal)

1. Introduction

As stellarators are becoming a viable option for a fusion reactor [1, 2], fluid codes are being extended to non-axisymmetric magnetic field geometries to study the properties of plasma turbulence in the stellarator boundary. BSTING, an extension of the BOUT++ code [3], simulated seeded filaments in a rotating ellipse [4]. More recently, the first global flux-driven simulations of a stellarator, performed by using the GBS code [5–7], considered a vacuum magnetic field generated with the Dommaschk potentials, reporting important differences with respect to tokamak simulations, namely the existence of a low-m mode, where m is the poloidal mode number, dominating the turbulent transport [8]. Such surprising result calls for the validation of turbulence simulations in stellarators.

In this paper, we present the first validation of a simulation of plasma turbulence in a stellarator configuration against experimental measurements. We compare helium discharges

* Author to whom any correspondence should be addressed.

Original Content from this work may be used under the terms of the Creative Commons Attribution 4.0 licence. Any further distribution of this work must maintain attribution to the author(s) and the title of the work, journal citation and DOI.

 © 2023 The Author(s). Published by IOP Publishing Ltd

carried out in the TJ-K stellarator with a simulation performed using the GBS code. TJ-K is a stellarator experiment ideally suited for a detailed comparison with simulations [9]. Because of the low plasma density and electron temperature, Langmuir probes can access the entire plasma volume and provide equilibrium as well as turbulence measurements that can be easily compared with simulations. In addition, since collisionality in TJ-K is large in the whole plasma volume, the fluid equations evolved by GBS are valid both in the core and in the boundary regions. Finally, the small size of the machine makes its simulation attractive from the point of view of the computational cost.

Previous turbulence modelling of TJ-K was accomplished either through modified Hasegawa-Wakatani models in slab geometry [10, 11] or by using a fluid model in a simplified geometry with the characteristic plasma parameters of TJ-K [12]. Due to their simplicity, a detailed one-to-one comparison of the simulations against experimental results was not attempted. The present work leverages previous validations of GBS against experiments carried out in axisymmetric configurations [13–16]. Thanks to the full-f nature of the GBS simulation code, which does not make a separation between background and fluctuations, we validate equilibrium as well as fluctuating quantities (density and electrostatic potential).

The paper is organized as follows. Section 2 describes the TJ-K experiment. In section 3, the physical model implemented in GBS is presented. In section 4, the simulation results are presented and their validation with the TJ-K experiment is reported. Finally, we discuss our results and draw our conclusions in section 5.

2. The TJ-K experiment

TJ-K is a six-field period stellarator with a major radius of 0.6 m and a minor radius of, approximately, 0.1 m [9]. The vacuum magnetic field is generated by a helical coil that loops around the vessel six times, and two vertical-field circular coils, as shown in figure 1. The magnetic field strength is, approximately, 70 mT. The Poincaré plots at four different toroidal angles are shown in figure 2 with the toroidal vessel depicted in grey. Continuous lines correspond to closed flux surfaces, while dashed lines correspond to open flux surfaces. The last closed flux surface (LCFS) is represented in red. In fact, the plasma is limited at the top and bottom part of the vessel at two different poloidal planes for every field period. The profile of the rotational transform is approximately flat, with a value $\iota = 0.28$ at the magnetic axis (henceforth defined by the coordinates R_{axis} and Z_{axis}, that vary along the toroidal angle ϕ).

In TJ-K, the plasma breakdown and heating is achieved with electron cyclotron resonant heating (ECRH), using a 2.45 GHz microwave system with up to 6 kW heating power [17]. When working with hydrogen or helium gases, this yields typical line-averaged plasma densities of order $10^{17}\,\text{m}^{-3}$ and the electron temperature around 10 eV, while ions are cold (the ion temperature is less than 1 eV). This results in a plasma collisionality $\nu^* \simeq 10$, with ν^* defined as the ratio between the trapped particle collision frequency and the banana bounce frequency. As a consequence, TJ-K plasmas are in the Pfirsch-Schlüter regime [18].

The TJ-K Langmuir probes enable measurements with good spatial resolution. The radial profiles of density and electron temperature are measured with a radially movable Langmuir probe, and the radial profile of the electrostatic potential with an emissive probe. In addition, density and plasma potential fluctuations are measured with two multi-probe arrays consisting of 64 Langmuir probes each, located at two different toroidal locations, one at an outer port at $\phi = 30°$ and the other at a top port at $\phi = 10°$. The probe tips are aligned to the same flux surface as shown in figure 1. This surface, referred to as the *reference surface* in the following, corresponds to the orange surface in the Poincaré plots of figure 2. These two arrays allow for detailed measurements of the potential and density fluctuations as a function of the poloidal angle, θ. In particular, the radial $E \times B$ turbulent particle flux is evaluated as

$$\Gamma^{\text{exp}}_{E\times B}(\theta_i) = \frac{1}{B_i}\left\langle -\frac{\widetilde{\Phi}_{\text{fl},i+1} - \widetilde{\Phi}_{\text{fl},i-1}}{2\Delta y}\widetilde{I}_{\text{sat},i}\right\rangle_t, \tag{1}$$

where $\widetilde{\Phi}_{\text{fl,i}}$ and $\widetilde{I}_{\text{sat,i}}$ are, respectively, the floating potential and ion saturation current fluctuations as measured by the ith probe at the poloidal position θ_i, B_i is the magnetic field strength at the same position, and $\Delta y \approx 8$mm is the distance between adjacent probe tips covering the flux surface. The 64 tips alternate between measurements of $\widetilde{\Phi}_{\text{fl}}$ and $\widetilde{I}_{\text{sat}}$, hence the tips $\{i-1, i, i+1\}$ are used to compute the flux at θ_i. The temporal average is carried out over 1024 ms of the data sampled at 1 MHz, resulting in a very small uncertainty of the mean value. Systematic errors due to possible probe misalignments can be estimated to have maximum relative values of 13% [19]. The use of the floating potential instead of the plasma potential in the evaluation of $\Gamma^{\text{exp}}_{E\times B}$ is justified by the negligible temperature fluctuations present in the experiment [20].

3. The GBS simulation

GBS [5–7] is a three-dimensional, global, two-fluid, flux-driven code that solves the drift-reduced Braginskii equations [21], valid in the high-collisionality regime that often characterizes the plasma boundary of magnetic fusion devices as well as the core of low-temperature devices such as TJ-K. GBS evolves all quantities in time, without separation between equilibrium and fluctuating parts. We consider here the cold ion and the electrostatic limits, we apply the Boussinesq approximation [5] and neglect gyroviscous terms as well as the coupling to the neutral dynamics [22]. Within these approximations, the drift-reduced model evolved by GBS for the simulation considered in this paper is:

$$\frac{\partial n}{\partial t} = -\frac{\rho_*^{-1}}{B}[\Phi, n] - \nabla_\parallel(nV_{\parallel e}) + \frac{2}{B}[C(p_e) - nC(\Phi)] + D_n\nabla_\perp^2 n + D_n^\parallel \nabla_\parallel^2 n + \mathcal{S}_n \tag{2}$$

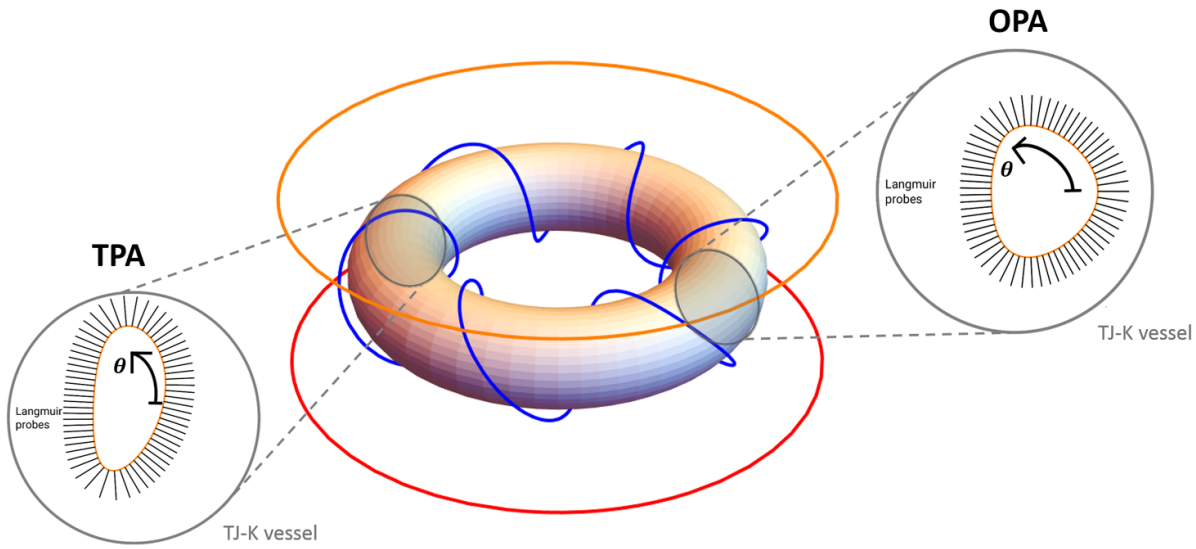

Figure 1. Schematics of the TJ-K experiment. The magnetic field is generated by a helical coil (blue) and two vertical-field circular coils (orange and red). Two multi-Langmuir probe arrays are distributed poloidally along the same flux surface at two different toroidal angles (TPA and OPA).

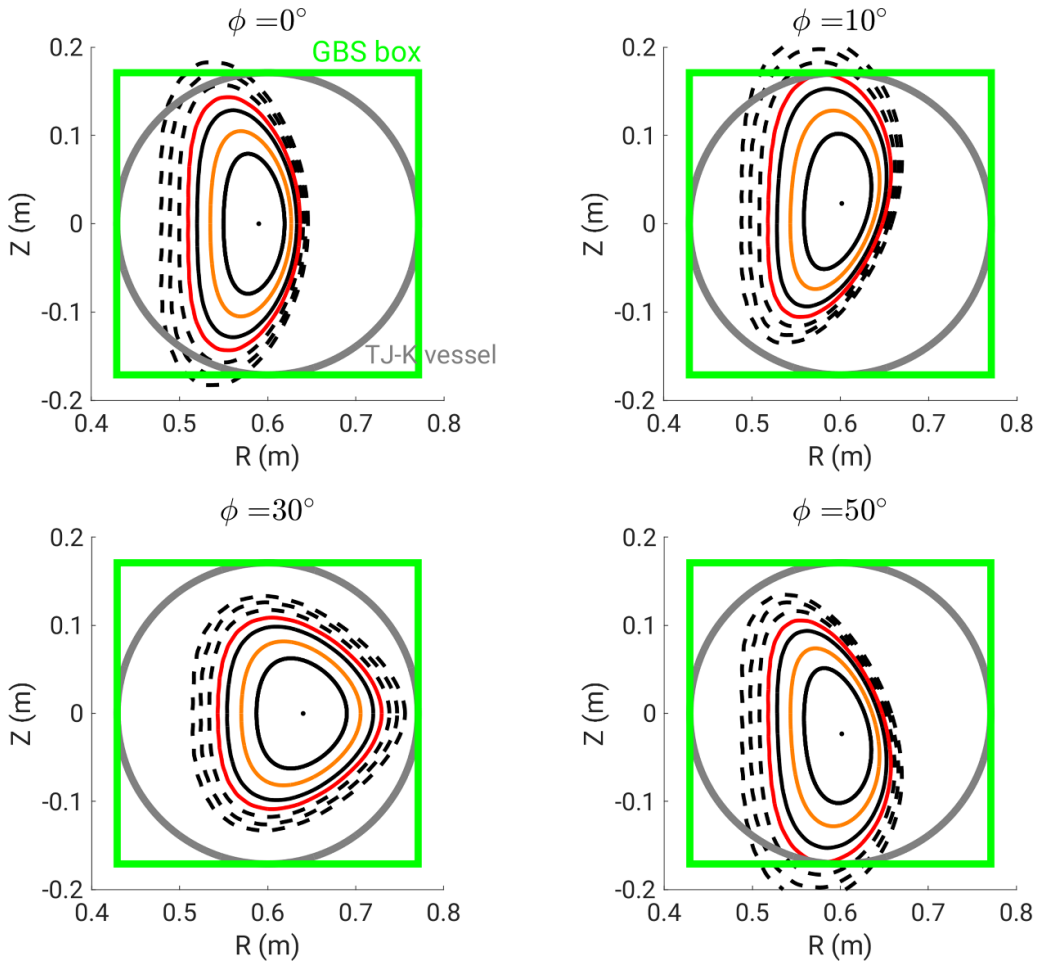

Figure 2. Poincaré plots of the TJ-K magnetic field at four different toroidal angles. The circular vessel is depicted in grey and the GBS simulation box in green. Closed flux surfaces are represented by continuous lines and open flux surfaces by dashed black lines. These are separated by the LCFS in red. The orange line refers to the surface where density and potential fluctuation measurements are performed (this is referred to as the *reference surface*).

$$\frac{\partial T_e}{\partial t} = -\frac{\rho_*^{-1}}{B}\left[\Phi, T_e\right] - V_{\parallel e}\nabla_\parallel T_e + \frac{4T_e}{3B}\left[\frac{C(p_e)}{n} + \frac{5}{2}C(T_e) - C(\Phi)\right] + \frac{2T_e}{3n}\left[0.71\nabla_\parallel j_\parallel - n\nabla_\parallel V_{\parallel e}\right] + D_{T_e}\nabla_\perp^2 T_e + \chi_{\parallel e}\nabla_\parallel^2 T_e + \mathcal{S}_{T_e} \tag{3}$$

$$\frac{\partial V_{\parallel e}}{\partial t} = -\frac{\rho_*^{-1}}{B}\left[\Phi, V_{\parallel e}\right] - V_{\parallel e}\nabla_\parallel V_{\parallel e} + \frac{m_i}{m_e}\left[\nu j_\parallel + \nabla_\parallel \Phi - \frac{\nabla_\parallel p_e}{n} - 0.71\nabla_\parallel T_e\right] + \eta_{0e}\nabla_\parallel^2 V_{\parallel e} + D_{V_{\parallel e}}\nabla_\perp^2 V_{\parallel e} \tag{4}$$

$$\frac{\partial V_{\parallel i}}{\partial t} = -\frac{\rho_*^{-1}}{B}\left[\Phi, V_{\parallel i}\right] - V_{\parallel i}\nabla_\parallel V_{\parallel i} - \frac{1}{n}\nabla_\parallel p_e + \eta_{0i}\nabla_\parallel^2 V_{\parallel i} + D_{V_{\parallel i}}\nabla_\perp^2 V_{\parallel i} \tag{5}$$

$$\frac{\partial \omega}{\partial t} = -\frac{\rho_*^{-1}}{B}\left[\Phi, \omega\right] - V_{\parallel i}\nabla_\parallel \omega + \frac{B^2}{n}\nabla_\parallel j_\parallel + \frac{2B}{n}C(p_e) + D_\omega \nabla_\perp^2 \omega + D_\omega^\parallel \nabla_\parallel^2 \omega \tag{6}$$

$$\nabla_\perp^2 \Phi = \omega. \tag{7}$$

In equations (2)–(7) all quantities are normalized to reference values. Density n and electron temperature T_e are normalized to the reference values n_0 and T_{e0}; electron parallel velocity $V_{\parallel e}$ and ion parallel velocity $V_{\parallel i}$ are both normalized to the sound speed $c_{s0} = \sqrt{T_{e0}/m_i}$; vorticity ω and the electrostatic potential Φ are normalized to $T_{e0}/(e\rho_{s0}^2)$ and T_{e0}/e; time is normalized to R_0/c_{s0}, where R_0 is the machine major radius; perpendicular and parallel lengths are normalized to the ion sound Larmor radius, $\rho_{s0} = \sqrt{T_{e0}m_i}/(eB_0)$, and R_0, respectively. The normalized parallel current is $j_\parallel = n(V_{\parallel i} - V_{\parallel e})$ and the magnetic field B is normalized to its norm at the magnetic axis, B_0.

The dimensionless parameters appearing in the equations are the normalized ion sound Larmor radius $\rho_* = \rho_{s0}/R_0$; the normalized electron and ion parallel diffusivities, $\chi_{\parallel e}$ and $\chi_{\parallel i}$ (here considered constant); the normalized electron and ion viscosities, η_{0e} and η_{0i}, which we also set to constant values; and the normalized Spitzer resistivity $\nu = \nu_0 T_e^{3/2}$ with ν_0 given in [23]. Small numerical diffusion terms such as $D_n\nabla_\perp^2 n$ and $D_n^\parallel \nabla_\parallel^2 n$ (and similar for the other fields) are introduced to improve the numerical stability of the code, and the simulation results show that they lead to significantly lower perpendicular transport than the turbulent one. The terms $\mathcal{S}_n$ and $\mathcal{S}_{T_e}$ denote the normalized sources of density and electron temperature. Magnetic presheath boundary conditions, described in [24, 25], are applied to all quantities at the end of the field lines intersecting the walls, except for density and vorticity. These satisfy $\partial_s n = 0$ and $\omega = 0$, respectively, where s is the direction normal to the wall.

The normalized geometrical operators appearing in equations (2)–(7) are the parallel gradient $\nabla_\parallel u = \boldsymbol{b}\cdot\boldsymbol{\nabla}u$, the Poisson brackets $[\Phi, u] = \boldsymbol{b}\cdot[\boldsymbol{\nabla}\Phi\times\boldsymbol{\nabla}u]$, the curvature operator $C(u) = (B/2)[\boldsymbol{\nabla}\times(\boldsymbol{b}/B)]\cdot\boldsymbol{\nabla}u$, the parallel Laplacian $\nabla_\parallel^2 u = \boldsymbol{b}\cdot\boldsymbol{\nabla}(\boldsymbol{b}\cdot\boldsymbol{\nabla}u)$ and the perpendicular Laplacian $\nabla_\perp^2 u = \boldsymbol{\nabla}\cdot[(\boldsymbol{b}\times\boldsymbol{\nabla}u)\times\boldsymbol{b}]$.

The simulation domain is a torus of radius R_0 with a rectangular cross-section. Since the vessel of the experiment has, instead, a circular cross-section, we choose the size of the domain in order to limit the plasma at the same positions as in the experiment. This simulation domain is shown in figure 2(green line). The physical model in equations (2)–(7) is discretized using a regular cylindrical grid (R, ϕ, Z), with R the radial coordinate, ϕ the toroidal angle and Z the vertical coordinate. Equations (2)–(6) are advanced in time with an explicit Runge-Kutta fourth-order scheme, while spatial derivatives are computed with a fourth-order finite difference scheme.

The magnetic field was initially computed numerically using the MAKEGRID code from the STELLOPT package [26], which uses the Biot-Savart law to determine the magnetic field at a specified location, using the coil geometry and coil currents as an input. However, since the vessel of the experiment, as well as the helical coil, fall inside the GBS domain, singularities in the magnetic field at the position of the coil appear, hindering an appropriate implementation of the geometrical operators. To circumvent this issue, we select one of the open flux surfaces (obtained with the FIELDLINES code from the same package) and provide it as an input to REGCOIL [27]. This code seeks a surface current distribution on an arbitrary toroidal surface, which we choose to enclose the GBS rectangular domain, such that $\mathbf{B}\cdot\mathbf{n} = 0$ at the provided surface. Furthermore, since $\nabla\times\mathbf{B} = 0$ in vacuum, the problem is reduced to a Laplace equation with Neumann boundary conditions, that admits a unique solution (up to a re-scaling factor). This results in a magnetic field obtained by REGCOIL that is exactly the same as that of TJ-K inside the chosen surface (apart from the re-scaling factor). With this approach, we obtain a non-singular vacuum magnetic field that coincides with that of TJ-K from the magnetic axis up to the selected open flux surface.

The degree of ionization at TJ-K is usually small, with the helium ionization fraction estimated below 12%. The impact of the electron-neutral collisions on the drift-reduced Braginskii model, in particular the parallel friction and parallel thermal conduction terms, can be assessed by quantifying the ratio ν_{en}/ν_{ei}, where ν_{ei} is the Coulomb electron-ion collision frequency [28] and $\nu_{en} = n_n\sigma_{en}v_{Te}$ is the electron-neutral collision frequency, with n_n the neutrals density, σ_{en} the momentum transfer cross-section for electrons impacting neutrals and v_{Te} the electron thermal velocity. With a working pressure of the plasma discharges considered here of 3 mPa and temperature of the neutrals gas between 300 and 600 K, n_n

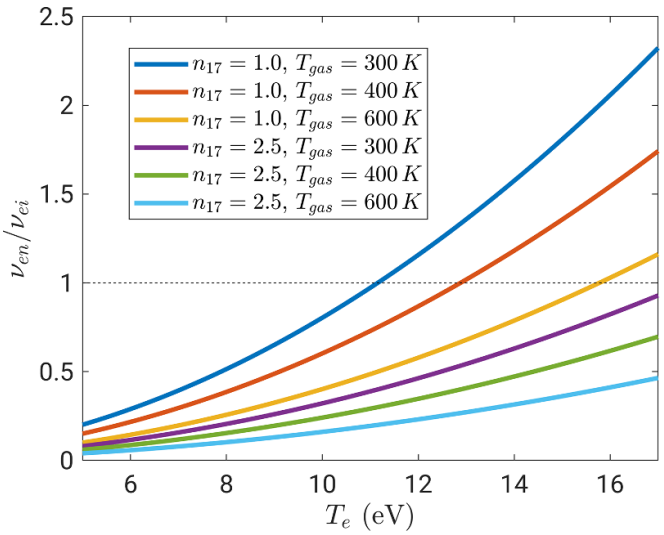

Figure 3. Ratio between electron-neutral and electron-ion collision frequencies at different plasma densities and gas temperatures, $T_{\rm gas}$. We indicate with n_{17} the plasma density in units of $10^{17}\,\mathrm{m}^{-3}$. The neutral pressure was assumed to be 3 mPa, the gas pressure of the TJ-K discharges presented in this paper.

is in the range (3.7–7.2) $\times\ 10^{17}\,\mathrm{m}^{-3}$. The ratio of the collision frequencies is shown in figure 3 for electron temperatures ranging between 5 eV and 17 eV, for which $\sigma_{en} \approx 10^{-19}\mathrm{m}^{-2}$ [29]. The different curves refer to different plasma densities and neutral temperatures, and show that the electron-neutrals interaction can become important at large electron temperatures. Nevertheless, in this work we assume that these interactions do not play a role. Regarding the ion-neutral interactions via charge-exchange, they are negligible with respect to the other terms appearing in the ion momentum equation, equation (5), in the range of ion temperatures of TJ-K. Another term neglected is the equipartition term in equation (3). This is justified by the fact that the equipartition occurs at a time scale of $\frac{m_i}{m_e}\tau_{ei} \sim 10^{-2}\,\mathrm{s}$, which is longer than the TJ-K energy confinement time, estimated to be around $10^{-3}\,\mathrm{s}$.

We consider that the source of density is due to ionization processes. This is modelled as $\mathcal{S}_n = n_n n \langle\sigma_{\rm ion} v\rangle_v$. The neutral pressure in TJ-K is approximately constant throughout the plasma volume, and ionization is due to fast electrons (whose density is assumed proportional to the plasma density) since the helium ionization cross-section peaks at an electron impacting energy much larger than the electron thermal energy. Hence, the density source is recast as $\mathcal{S}_n = \alpha_n n$, with α_n a constant. We neglect recombination processes because of the typical TJ-K temperatures.

The electron temperature source is composed of the external energy input power and a sink term associated with the particle source, leading to

$$\mathcal{S}_{Te} = \frac{R_0/c_{s0}}{T_{e0}}\left[\frac{2}{3}\frac{\mathcal{P}}{n_0 n} - \frac{2}{3}n_n\langle\sigma v\rangle_{\rm ion}\left(E_{\rm ion} + \frac{3}{2}T_{e0}T_e\right)\right], \quad (8)$$

where $\mathcal{P}$ is the ECRH input power density, $\langle\sigma v\rangle_{\rm ion}$ is the ionization reaction-rate, which is of the order of $10^{-15}\,\mathrm{m}^3\,\mathrm{s}^{-1}$ at 10 eV [30], and $E_{\rm ion}$ is the ionization energy. As described in [17], power deposition in TJ-K occurs at the upper hybrid (UH) resonance layer. The space-dependent input power $\mathcal{P}$ is given by

$$\mathcal{P} = \frac{\mathcal{P}_{\rm ant}}{\int_V P(\mathbf{r})\mathrm{d}\mathbf{r}}P(\mathbf{r}), \quad (9)$$

where $\mathcal{P}_{\rm ant} = 1.8$ kW is the power launched by the antennas in the TJ-K discharges considered here and $P(\mathbf{r})$ is the UH resonant layer, shown in figure 4 at different poloidal planes. $P(\mathbf{r})$ is obtained by matching the UH frequency with the antenna frequency, $\sqrt{\omega_{\rm pe}^2 + \omega_{\rm ce}^2} = 2\pi f_{\rm antenna}$, and then assuming a Gaussian deposition profile with a width of 5 mm located around the isocountours that solve this relation. This results into $\int_V P(\mathbf{r})\mathrm{d}\mathbf{r} = 0.0163$. The temperature source in equation (8) can thus be written as

$$\mathcal{S}_{Te} = \frac{R_0/c_{s0}}{T_{e0}}\frac{2}{3}\left[\frac{\mathcal{P}_{\rm ant}}{n_0\int_V P(\mathbf{r})\mathrm{d}\mathbf{r}}\frac{P(\mathbf{r})}{n} - n_n\langle\sigma v\rangle_{\rm ion}E_{\rm ion}\left(1 + \frac{3}{2}\frac{T_{e0}T_e}{E_{\rm ion}}\right)\right]. \quad (10)$$

For helium we consider the first ionization energy, $E_{\rm ion} = 24.6$ eV. Since $T_{e0} = 10$ eV, we can further approximate $\frac{3}{2}T_{e0} \approx E_{\rm ion}$. Finally, since $n_0 = 10^{17}\,\mathrm{m}^{-3}$, the previous expression is recast as:

$$\mathcal{S}_{Te} = \alpha_{Te}\left[\frac{P(\mathbf{r})}{n} - 3\times10^{-4}E_{\rm ion}^{\rm eV}(1+T_e)\right]. \quad (11)$$

The constants α_n and α_{Te} are adjusted such that the peak values of density and temperature are close to the reference values, $n \approx 1$ and $T_e \approx 1$. This adjustment accounts for the uncertainties on the averaging of the ionization reaction-rate and on the effective absorption by the plasma of the ECRH power.

Turning now to the simulation parameters, we consider $\rho_*^{-1} = 60$ and $\nu_0 = 5\times10^{-4}$ by using the reference values $T_{e0} = 10$ eV and $n_0 = 10^{17}\ \mathrm{m}^{-3}$. We use an atomic number $Z = 1$ since helium is mostly single-ionized at the reference temperature. We further use $m_i/m_e = 900$, $\chi_{\parallel e} = 0.5$, $\eta_{0e,i} = 1.0$, $D_n = D_{Te} = D_{V_{\parallel e}} = D_{V_{\parallel i}} = D_\omega = 0.2$, $D_n^{\parallel} = 0.18$, $D_\omega^{\parallel} = 0.01$, $\alpha_n = 0.03$ and $\alpha_{Te} = 0.7$. Concerning the numerical parameters, the simulation is performed with a time-step of $2.0\times10^{-5}R_0/c_{s0}$ and a grid resolution of $\Delta R = \Delta Z = 0.5\rho_{s0}$ and $\Delta\phi = 2\pi/(20\times6)$, i.e. 20 poloidal planes per field period. A convergence test in the toroidal direction, made by increasing the number of planes from 20 to 30 per field period, show results similar to the one presented here.

The simulation of TJ-K we consider is started from an initial state with background noise and, after a transient, reaches a quasi-steady state where sources, parallel and perpendicular transport, and losses at the vessel balance each other. The analysis of the simulations results is performed during this quasi-steady state.

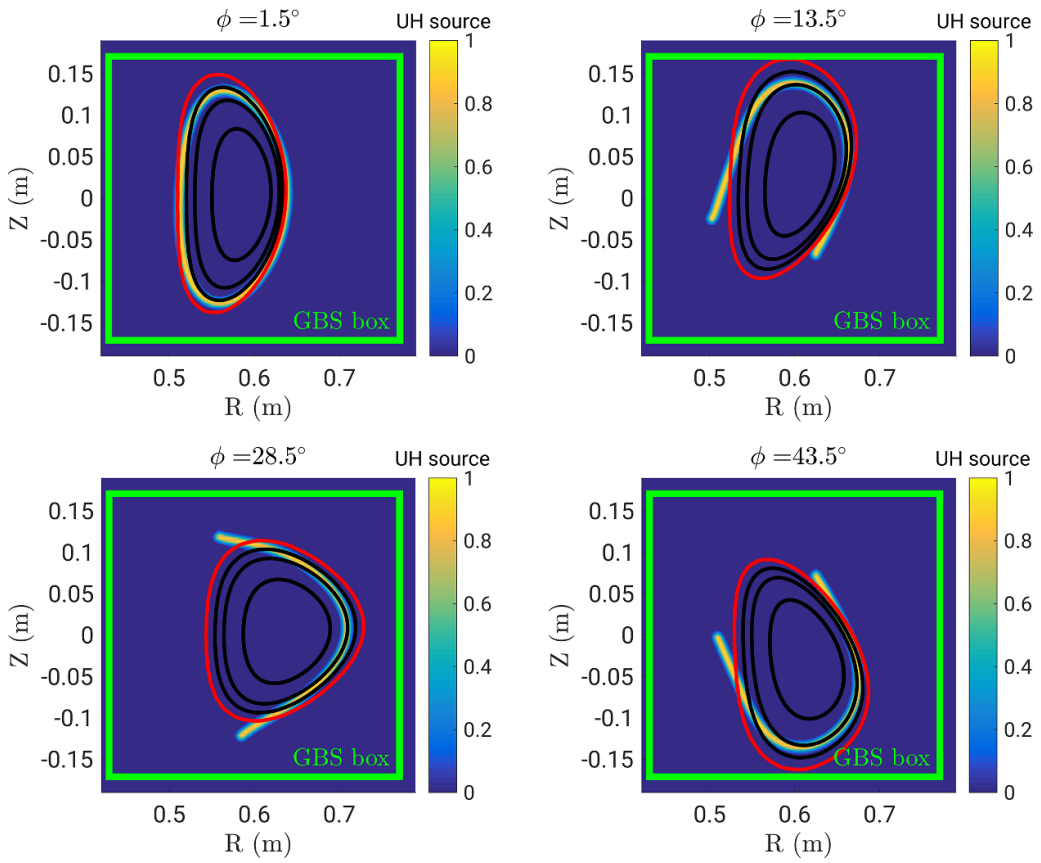

Figure 4. The UH resonant layer, $P(\mathbf{r})$, considered in the simulation. The layer is obtained by matching the UH frequency with the frequency of the antenna, $\sqrt{\omega_{\rm pe}^2+\omega_{\rm ce}^2}=2\pi f_{\rm antenna}$, being $f_{\rm antenna}=2.45$ GHz.

4. Simulation results and comparison with the experiment

We start by comparing the one-dimensional time-averaged (equilibrium) profiles of density, temperature, potential and radial electric field, $E_R=-\nabla\Phi\cdot\widehat{\mathbf{e}}_{\mathbf{R}}$, along the R direction, at $Z=0$ and $\phi=30°$. The comparison is shown in figure 5. The peak value as well as the profile of the simulated density agree well with the experiment. The experimental temperature profile is hollow and this is attributed to the fact that the resonance layer of the UH is located at the edge (see figure 4). On the other hand, the simulation displays a temperature profile that decays for $R>R_{\rm axis}$. Furthermore, the temperature on axis is larger in the simulation than in the experiment. We note that the simulated temperature profile is sensitive to α_{Te}. Reducing this parameter lowers the value of the temperature, but the equilibrium gradients change, eventually suppressing turbulence. The magnitude of the electrostatic plasma potential is similar in both experiment and simulation (between 8 and 14 V), but the radial dependencies are different. In fact, the simulation reveals a hollow potential profile, whereas in the experiment the profile increases as the axis is approached. This makes the profiles of E_R also different, even if its order of magnitude is correctly captured.

Snapshots of the density and electrostatic potential on two different poloidal planes, $\phi=10°$ and $\phi=30°$, are shown in figure 6. We observe that a low-m coherent mode dominates the plasma dynamics, where m is the poloidal mode number. We Fourier decompose the fluctuations along the y-coordinate, where y is the arc length along the poloidal projection of the reference surface. Figure 7(left) shows the power spectrum of density fluctuations obtained at $\phi=30°$ and compares it with the experiment. All simulation spectra presented here are averaged over a time window of, approximately, 18 time units, ensuring the statistical convergence of the results. The simulation retrieves the coherent mode present in the experiment at $k_y\rho_{s0}\approx0.4$, which corresponds to an $m=4$ structure. The experimental spectrum decays with a power law $(k_y\rho_{s0})^{-1.9}$, consistent with the inverse cascade in two-dimensional fluid turbulence [31]. On the other hand, the observed power law in the simulation, $(k_y\rho_{s0})^{-2.8}$, is overestimated with respect to the experiment. The power spectrum at $\phi=10°$ (not shown) is similar to the one at $\phi=30°$, both in the experiment and simulation, an expected feature since turbulence is field-aligned. Regarding the power spectrum of the electrostatic potential (right panel in figure 7), the simulation has two dominant coherent modes at $k_y\rho_{s0}\approx0.4$ and $k_y\rho_{s0}\approx0.7$, although only the first one is present in the experiment.

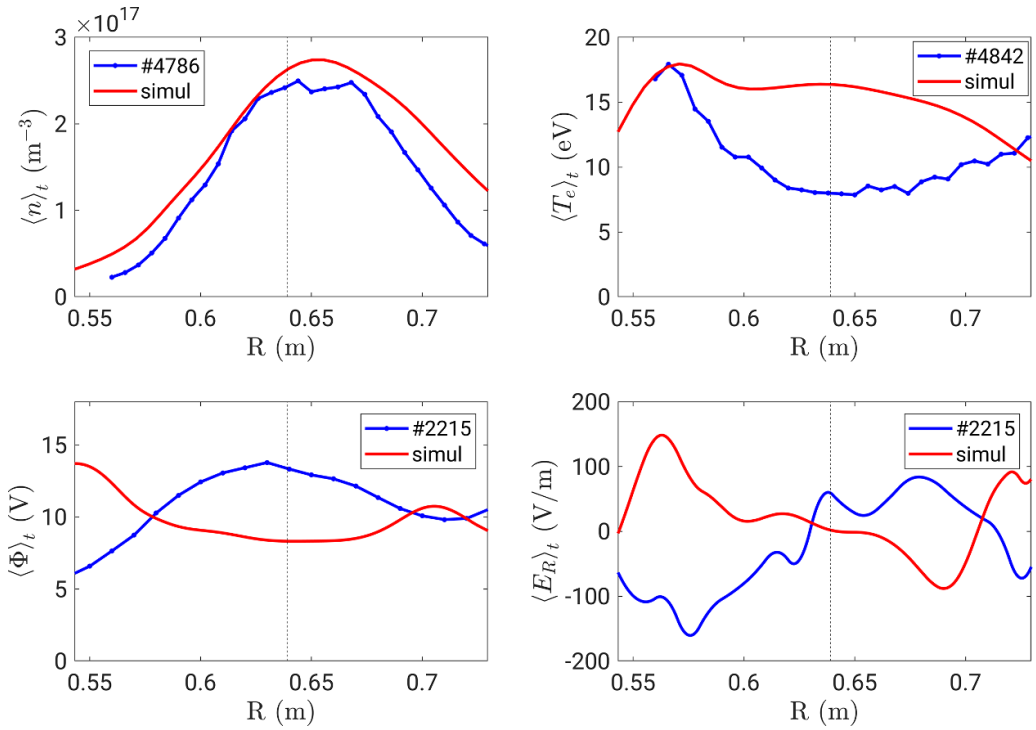

Figure 5. Radial profiles of the time-averaged (equilibrium) density, electron temperature, potential and radial electric field. Profiles are at $Z = 0$ and $\phi = 30^\circ$ (OPA). The vertical dashed line indicates the position of the magnetic axis, R_{axis}.

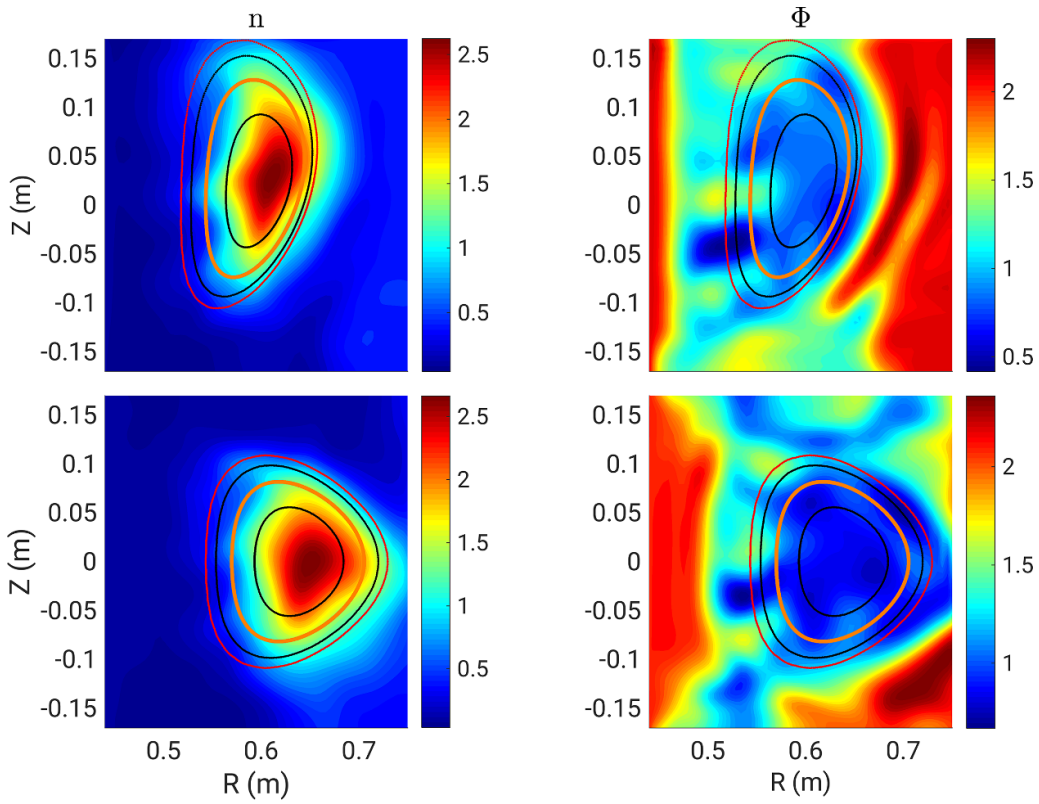

Figure 6. Snapshot of density, n (left) and electrostatic potential, Φ (right), in the quasi-steady state of the GBS simulation. Top and bottom correspond to the toroidal planes $\phi = 10^\circ$ (TPA) and $\phi = 30^\circ$ (OPA), respectively. The reference surface is indicated with an orange line.

In addition, the simulation spectrum shows a faster decay in the simulation than in the experiment, as in the density case.

In figure 8, we show the density and potential fluctuation levels as a function of the poloidal angle on the reference surface, for the two considered poloidal planes. The fluctuation

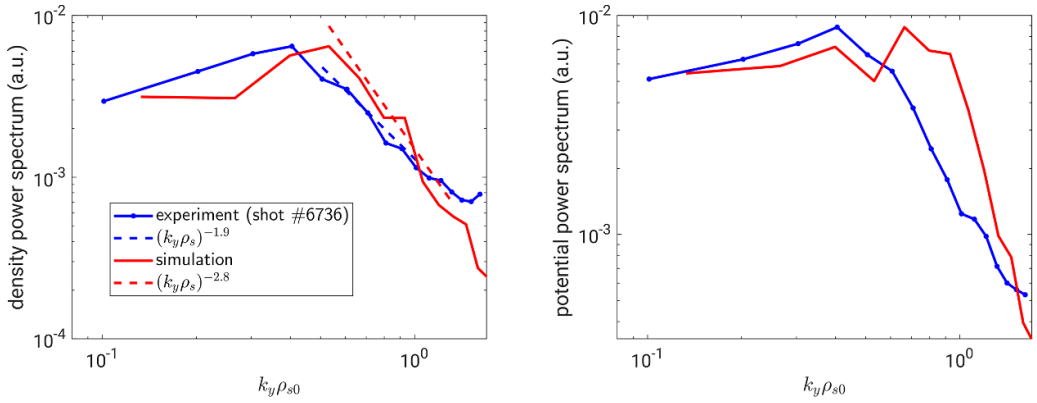

Figure 7. Power spectrum of density (left) and electrostatic potential (right) of the fluctuations. The spectra are computed by Fourier transforming density fluctuations along y at OPA ($\phi = 30°$). The simulation spectrum is normalized such that the maxima of experiment and simulation are the same.

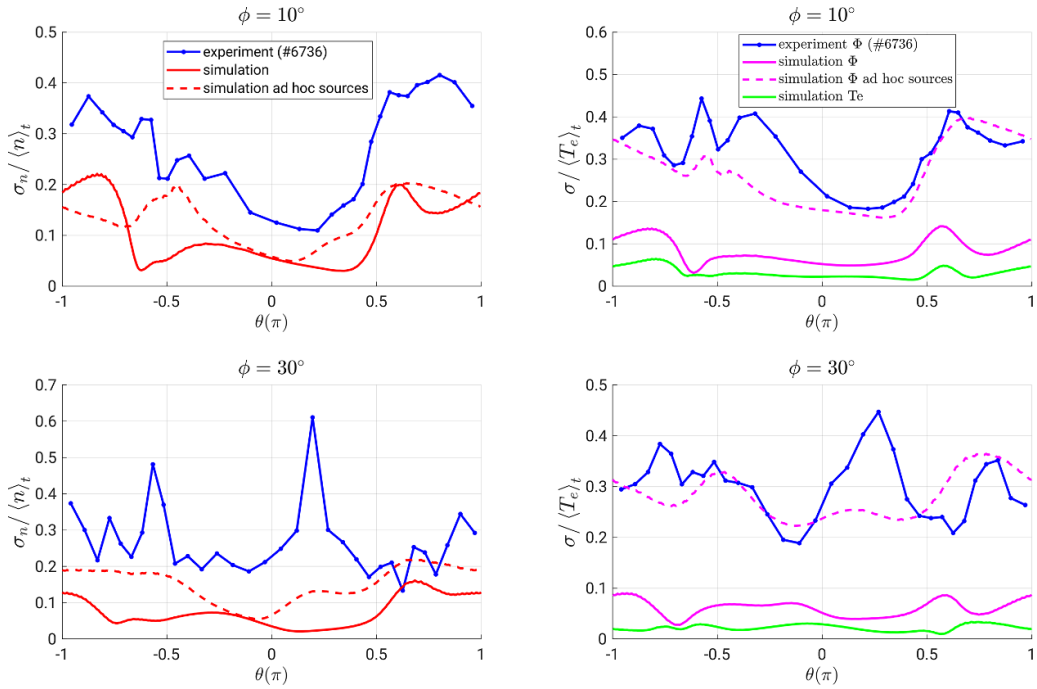

Figure 8. Density (left) and potential and electron temperature (right) fluctuation levels as a function of the poloidal angle, θ, at $\phi = 10°$ (top) and $\phi = 30°$ (bottom). The dashed lines correspond to the fluctuation levels obtained with the ad hoc sources shown in figure 9.

level of the density is calculated as the standard deviation, σ_n, normalized to the radially dependent equilibrium value, $\langle n\rangle_t$. The normalizing factor of the potential is the equilibrium electron temperature, $\langle T_e\rangle_t$, to avoid possible singularities. The simulation and experiment display a similar poloidal dependence at $\phi = 10°$. However, the simulation underestimates the fluctuation levels by a factor two or more. This is similar to previous validation studies with GBS and other fluid codes, where a lower level of fluctuations with respect to experiments is reported [15, 16]. At $\phi = 30°$, the simulated fluctuations are also significantly smaller than in the experiment and, in addition, fluctuations do not peak at the same poloidal angle. Regarding electron temperature fluctuations, they are negligible in TJ-K [20]. In the simulation, although not being negligible, they are smaller than density and potential fluctuations, as demonstrated in figure 8.

We note that both the spectrum and the fluctuation levels are robust to the source localization and strength. In fact, a simulation was carried out with density and temperature ad hoc sources, $\mathcal{S}_{adhoc}$, of equal magnitude and localized around a closed flux surface in the proximity of the LCFS, as shown in figure 9. For comparison, we show in figure 10 the time-averaged sources $\langle \mathcal{S}_n\rangle_t$ and $\langle \mathcal{S}_{Te}\rangle_t$. The density fluctuation levels obtained in the simulation with an ad hoc source are very similar to the ones obtained with more realistic sources, as shown on figure 8(dashed lines of the plots on the left). Regarding the fluctuation levels of the potential, its amplitude is closer to the experimental one,

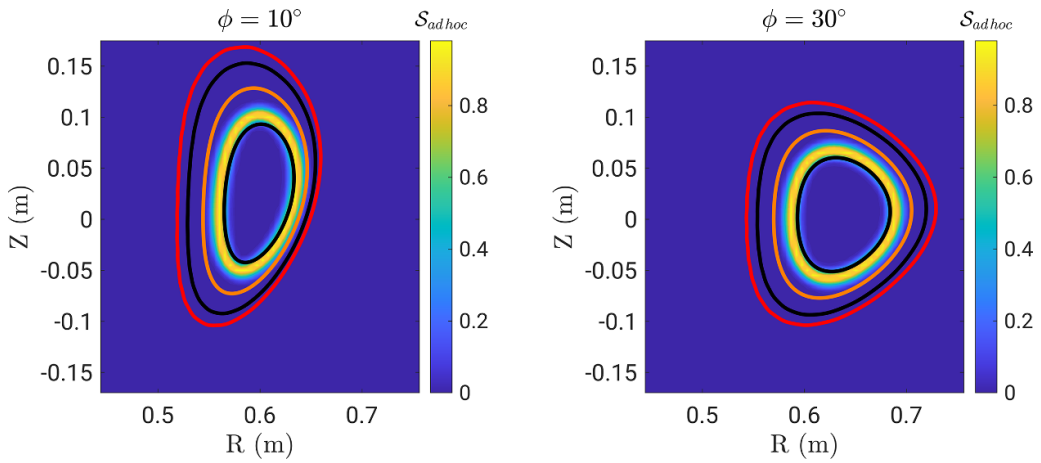

Figure 9. Ad hoc density and temperature sources on two different poloidal planes.

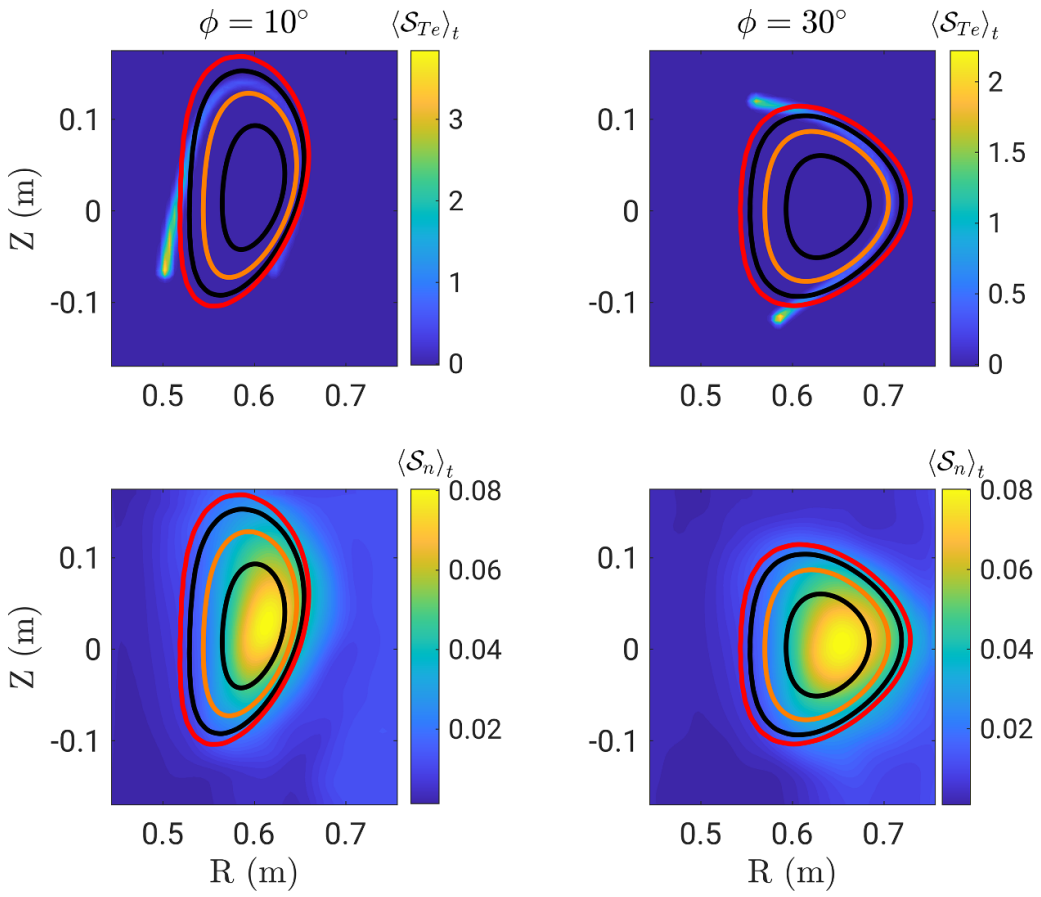

Figure 10. Time-averaged density and temperature sources used in the simulation presented in this paper.

although at $\phi = 30°$ the major peak is not retrieved. It should be mentioned that the spectrum obtained with the ad hoc sources, not shown here, is similar to the one presented in figure 7.

The simulated radial turbulent $E \times B$ particle flux,

$$\Gamma_{E\times B} = \left\langle \widetilde{n}\widetilde{V}^r_{E\times B} \right\rangle_t = -\left\langle \frac{\widetilde{n}}{B}\left(\nabla\widetilde{\Phi}\times\mathbf{b}\right)_r \right\rangle_t, \qquad (12)$$

where r denotes the direction normal to the flux surface, is compared with the experiment. The comparison is shown in figure 11. Both fluxes are normalized to their peak values since the experimental value of transport is based on the ion saturation current. The simulation and experimental results at $\phi = 10°$ agree considerably better than at $\phi = 30°$. At $\phi = 10°$ the simulation retrieves the transport peak occurring at around $\theta = \pi/2$, while the peak at $\theta = 0.2\pi$ is not retrieved at

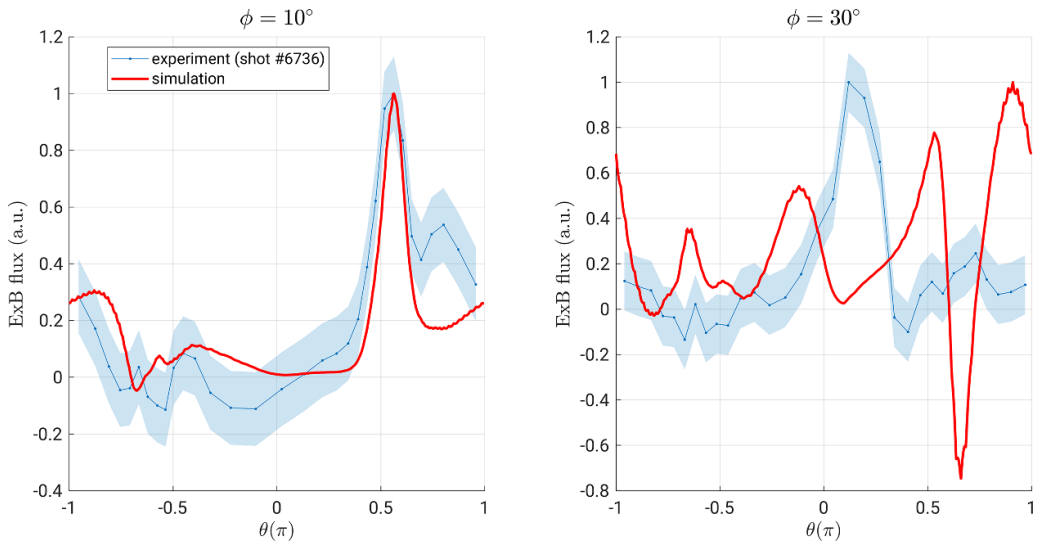

Figure 11. Comparison of the $E \times B$ flux as given by experiment and simulation at $\phi = 10°$ (TPA) and $\phi = 30°$ (OPA).

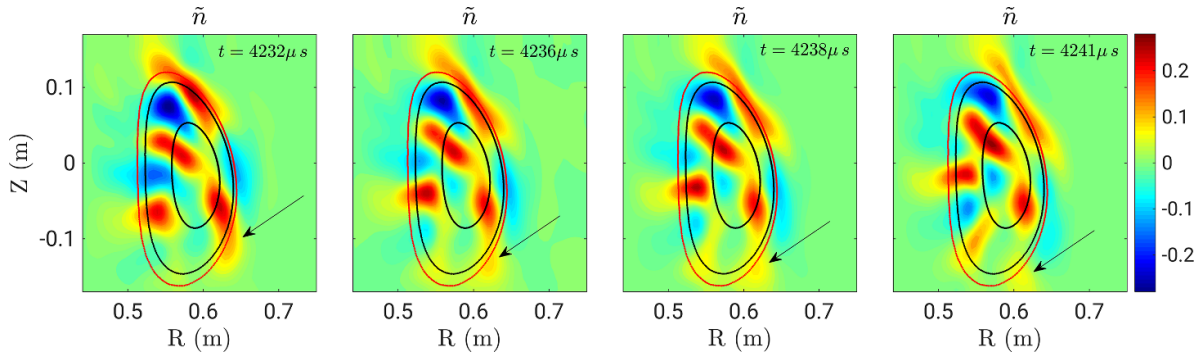

Figure 12. Time sequence of density fluctuations in the simulation. The arrow points to a region where a large coherent structure, originated inside the LCFS, detaches and propagates towards the SOL within a few μs.

$\phi = 30°$. This is partially explained by the different peak position of the fluctuation levels observed at $\phi = 30°$ (see figure 8). In addition, the cross-phase has an important role in setting the level of transport. In fact, the simulation shows a peak of the flux with a negative value, revealing that the phase-difference between density and potential also varies poloidally, hence having an important role in the turbulent transport asymmetries. It is worth mentioning that in the experiment there is a good correlation between the position where turbulent transport is maximum and the region where normal and geodesic curvatures are, respectively, negative and positive [19], something that could not be verified with the simulations.

Coherent structures originating from inside the LCFS and propagating outwards into the scrape-off layer (SOL) are typically observed in TJ-K by means of a 2D movable probe and/or a fast camera [32–34]. The origin of these structures is attributed to drift-waves turbulence. The presence of coherent structures propagating from the closed field line region towards the SOL is visible also in the simulation. This is shown in figure 12, where a time sequence of the density fluctuations is shown. The formation of this coherent structure occurs in the region marked with an arrow within a few μs, as in the experiments [32, 33].

5. Discussion and conclusions

GBS captures the essential turbulence properties of TJ-K, for instance the k_y spectra, as shown in figure 7. In addition, although not presented in this paper, a simulation with an hydrogen plasma also shows good agreement with the experimental k_y spectrum.

The equilibrium profiles of temperature, potential and electric field, which reveal significant differences between simulations and experiments, depend significantly on the details of the sources, whose localization and strength are, to some extent, uncertain. For example, using the ad hoc sources lead to an order magnitude difference of the E_R values between simulation and experiment.

The fact that GBS is able to retrieve the experimental density profile shows that *globally* the code is able to capture the turbulent transport of TJ-K. Here *globally* is to be

understood in the sense of flux-surface integral of the turbulent flux. However, not all the details of the profile of the flux are well captured, at least in one of the two planes where experimental data is available. There is no incongruity here since, for the purpose of *global* transport (which is what determines the density profile), the flux-surface average is what matters and not the exact details of the flux.

The origin of the electric field is unclear, both in the experiment and in the simulation. Since the ion temperature is small, neoclassical effects do not play a role in setting the electric field, in contrast to the case of high temperature stellarator plasmas [35]. Moreover, a test where finite ion temperature effects are introduced in the system by setting $T_{i0}/T_{e0} = 0.1$ as in the experiment, shows similar results to the cold ion simulation. We expect that an improvement of the source model could yield a better agreement between simulation and experimental radial electric field. In fact, plasma breakdown in TJ-K occurs at the electron cyclotron resonance layer [36], and therefore the fast electrons produced at this resonance are responsible for the further ionization of the background gas. A proper modelling of this species could thus improve our comparison. Furthermore, as shown in figure 3, electron-neutrals interaction can become important at temperatures larger than 10 eV. Since TJ-K temperatures are between 8 eV and 17 eV (see figure 5), it might be important to take into account such interactions in future investigations.

Finally, we note that the role of boundary conditions is expected to be important in simulation of such small experiments such as TJ-K. The use of magnetic pre-sheath boundary conditions except for density and vorticity at the interface between the LCFS and the wall could affect the plasma dynamics and, for example, the peaking positions of the fluctuation levels.

To conclude, in this paper we present the first validation of the GBS code with a stellarator experiment. Overall, GBS captures the main features of turbulence, in particular the k_y spectrum. The fluctuation levels are underestimated but their dependence on the poloidal angle is partially retrieved. Regarding the equilibrium quantities, GBS can retrieve the correct magnitudes of the potential and electric field, whose profiles are sensitive to the strength and localization of the sources. The equilibrium density profile agrees well with the experiment, but in the case of the electron temperature the value on axis is underestimated. As experimentally observed in TJ-K and confirmed by the GBS simulations presented here, the turbulent transport is mainly due to a low-m mode, something that was also recently observed in an GBS simulation of a stellarator with an island divertor [8]. This contrasts with the typical plasma turbulence in tokamaks, where more broadband turbulence is observed. Ultimately, the validation of the presence of these low-m modes calls for the detailed study of the difference between stellarators and tokamaks.

Data availability statement

The data cannot be made publicly available upon publication because they are not available in a format that is sufficiently accessible or reusable by other researchers. The data that support the findings of this study are available upon reasonable request from the authors.

Acknowledgment

The authors thank Caoxiang Zhu and Matt Landreman for all the help with REGCOIL. The simulations presented herein were carried out in part at the Swiss National Supercomputing Centre (CSCS) under the Projects ID s1118 and s1182, and in part on the CINECA Marconi super computer. This work has been carried out within the framework of the EUROfusion Consortium, via the Euratom Research and Training Programme (Grant Agreement No. 101052200 - EUROfusion) and funded by the Swiss State Secretariat for Education, Research and Innovation (SERI). Views and opinions expressed are however those of the author(s) only and do not necessarily reflect those of the European Union, the European Commission, or SERI. Neither the European Union nor the European Commission nor SERI can be held responsible for them.

ORCID iDs

A J Coelho https://orcid.org/0000-0002-8889-7259
A Köhn-Seemann https://orcid.org/0000-0002-1192-2057
K Rahbarnia https://orcid.org/0000-0002-5550-1801

References

[1] Pedersen T S *et al* 2022 Experimental confirmation of efficient island divertor operation and successful neoclassical transport optimization in Wendelstein 7-X *Nucl. Fusion* **62** 042022
[2] Beidler C D *et al* 2021 Demonstration of reduced neoclassical energy transport in Wendelstein 7-X *Nature* **596** 221–6
[3] Shanahan B W, Hill P and Dudson B D 2016 Towards nonaxisymmetry; initial results using the Flux Coordinate Independent method in BOUT++ *J. Phys.: Conf. Ser.* **775** 012012
[4] Shanahan B W, Dudson B D and Hill P 2019 Fluid simulations of plasma filaments in stellarator geometries with BSTING *Plasma Phys. Control. Fusion* **61** 025007
[5] Ricci P, Halpern F D, Jolliet S, Loizu J, Mosetto A, Fasoli A, Furno I and Theiler C 2012 Simulation of plasma turbulence in scrape-off layer conditions: the GBS code, simulation results and code validation *Plasma Phys. Control. Fusion* **54** 124047
[6] Giacomin M *et al* 2022 The GBS code for the self-consistent simulation of plasma turbulence and kinetic neutral dynamics in the tokamak boundary *J. Comput. Phys.* **464** 111294
[7] Halpern F D *et al* 2016 The GBS code for tokamak scrape-off layer simulations *J. Comput. Phys.* **315** 388
[8] Coelho A J, Loizu J, Ricci P and Giacomin M 2022 Global fluid simulation of plasma turbulence in a stellarator with an island divertor *Nucl. Fusion* **62** 074004
[9] Krause N, Lechte C, Stöber J, Stroth U, Ascasibar E, Alonso J and Niedner S 2002 The Torsatron TJ-K, an experiment for the investigation of turbulence in a toroidal low-temperature plasma *Rev. Sci. Instrum.* **73** 10

[10] Garland S, Reuther K, Ramisch M and Manz P 2017 The collisionality dependence of intermittency level in drift-wave turbulence in the stellarator TJ-K *Phys. Plasmas* **24** 112307
[11] Garland S, Manz P and Ramisch M 2020 The influence of magnetic field curvature on intermittency in drift-wave turbulence in the stellarator TJ-K *Phys. Plasmas* **27** 052304
[12] Niedner S, Scott B D and Stroth U 2002 Statistical properties of drift wave turbulence in low-temperature plasmas *Plasma Phys. Control. Fusion* **44** 397–408
[13] Ricci P, Theiler C, Fasoli A, Furno I, Gustafson K, Iraji D and Loizu J 2011 Methodology for turbulence code validation: quantification of simulation-experiment agreement and application to the TORPEX experiment *Phys. Plasmas* **18** 032109
[14] Ricci P, Riva F, Theiler C, Fasoli A, Furno I, Halpern F D and Loizu J 2015 Approaching the investigation of plasma turbulence through a rigorous verification and validation procedure: a practical example *Phys. Plasmas* **22** 055704
[15] Galassi D *et al* 2022 Validation of edge turbulence codes in a magnetic X-point scenario in TORPEX *Phys. Plasmas* **29** 012501
[16] Oliveira D S *et al* 2022 Validation of edge turbulence codes against the TCV-X21 diverted L-mode reference case *Nucl. Fusion* **62** 096001
[17] Kohn A *et al* 2010 Generation and heating of toroidally confined overdense plasmas with 2.45 GHz microwaves *Plasma Phys. Control. Fusion* **52** 035003
[18] Helander P and Sigmar D J 2005 *Collisional Transport in Magnetized Plasmas* (Cambridge University Press)
[19] Birkenmeier G, Ramisch M, Manz P, Nold B and Stroth U 2011 Experimental investigation of the magnetic configuration dependence of turbulent transport *Phys. Rev. Lett.* **107** 255001
[20] Mahdizadeh N, Greiner F, Ramisch M, Stroth U, Guttenfelder W, Lechte C and Rahbarnia K 2005 Comparison of Langmuir and emissive probes as diagnostics for turbulence studies in the low-temperature plasma of the torsatron TJ-K *Plasma Phys. Control. Fusion* **47** 569
[21] Zeiler A 1999 Tokamak edge turbulence (Max-Planck-Institut für Plasmaphysik, IPP) 5/88
[22] Wersal C and Ricci P 2015 A first-principles self-consistent model of plasma turbulence and kinetic neutral dynamics in the tokamak scrape-off layer *Nucl. Fusion* **55** 123014
[23] Giacomin M and Ricci P 2020 Investigation of turbulent transport regimes in the tokamak edge by using two-fluid simulations *J. Plasma Phys.* **86** 905860502
[24] Loizu J, Ricci P, Halpern F D and Jolliet S 2012 Boundary conditions for plasma fluid models at the magnetic presheath entrance *Phys. Plasmas* **19** 122307
[25] Mosetto A, Halpern F D, Jolliet S, Loizu J and Ricci P 2015 Finite ion-temperature effects on scrape-off layer turbulence *Phys. Plasmas* **22** 012308
[26] MAKEGRID (available at: https://princetonuniversity.github.io/STELLOPT/MAKEGRID.html)
[27] Landreman M 2017 An improved current potential method for fastcomputation of stellarator coil shapes *Nucl. Fusion* **57** 046003
[28] Braginskii S I 1965 Transport processes in a plasma *Rev. Plasma Phys.* **1** 205
[29] Michels H H, Harris F E and Scolsky R M 1969 Calculation of cross-sections for electron-helium collisions *Phys. Lett.* A **28** 467–8
[30] Lechte C, Stöber J and Stroth U 2002 Plasma parameter limits of magnetically confined low temperature plasmas from a combined particle and power balance *Phys. Plasmas* **9** 2839
[31] Ramisch M, Manz P, Stroth U, Birkenmeier G, Enge S, Holzhauer E, Kohn A and Nold B 2010 Non-linear dynamics and plasma flows in a basic toroidal plasma experiment *Plasma Phys. Control. Fusion* **52** 124015
[32] Happel T, Greiner F, Mahdizadeh N, Nold B, Ramisch M and Stroth U 2009 Generation of intermittent turbulent events at the transition from closed to open field lines in a toroidal plasma *Phys. Rev. Lett.* **102** 255001
[33] Fuchert G, Birkenmeier G, Nold B, Ramisch M and Stroth U 2013 The influence of plasma edge dynamics on blob properties in the stellarator TJ-K *Plasma Phys. Control. Fusion* **55** 125002
[34] Fuchert G, Birkenmeier G, Ramisch M and Stroth U 2016 Characterization of the blob generation region and blobby transport in a stellarator *Plasma Phys. Control. Fusion* **58** 054005
[35] Simakov A N and Helander P 2009 Neoclassical momentum transport in a collisional stellarator and a rippled tokamak *Phys. Plasmas* **16** 042503
[36] Birkenmeier G, Höhnle H, Köhn A, Ramisch M and Stroth U 2008 Plasma start-up measurements in the toroidal plasma experiment TJ-K *IEEE Trans. Plasma Sci.* **36** 1092